

# JGR Earth Surface

## RESEARCH ARTICLE

10.1029/2020JF005601

### Key Points:

- Two-dimensional measurements of ooid size and shape are inaccurate and imprecise
- Ooids are powerful paleoenvironmental indicators, but only if they are measured in three dimensions
- Three-dimensional reconstructions of ooid growth histories can provide insights into the environments that formed giant ooids

### Supporting Information:

Supporting Information may be found in the online version of this article.

### Correspondence to:

B. Howes,  
[bhowes@princeton.edu](mailto:bhowes@princeton.edu)

### Citation:

Howes, B., Mehra, A., & Maloof, A. (2021). Three-dimensional morphometry of ooids in oolites: A new tool for more accurate and precise paleoenvironmental interpretation. *Journal of Geophysical Research: Earth Surface*, 126, e2020JF005601. <https://doi.org/10.1029/2020JF005601>

Received 10 MAR 2020

Accepted 10 FEB 2021

© 2021. American Geophysical Union.  
 All Rights Reserved.

## Three-Dimensional Morphometry of Ooids in Oolites: A New Tool for More Accurate and Precise Paleoenvironmental Interpretation

Bolton Howes<sup>1</sup> , Akshay Mehra<sup>1,2</sup>, and Adam Maloof<sup>1</sup>

<sup>1</sup>Department of Geosciences, Princeton University, Princeton, NJ, USA, <sup>2</sup>Department of Earth Sciences, Dartmouth College, Hanover, NH, USA

**Abstract** The prevalence of ooids in the stratigraphic record, and their association with shallow-water carbonate environments, make ooids an important paleoenvironmental indicator. Recent advances in the theoretical understanding of ooid morphology, along with empirical studies from Turks and Caicos, Great Salt Lake, and The Bahamas, have demonstrated that the morphology of ooids is indicative of depositional environment and hydraulic conditions. To apply this knowledge from modern environments to the stratigraphic record of Earth's history, researchers measure the size and shape of lithified ooids on two-dimensional surfaces (i.e., thin sections), often assuming that random 2D slices intersect the nuclei and that the orientation of the ooids is known. Here, we demonstrate that these assumptions rarely are true, resulting in errors of up to 35% for metrics like major axis length. We present a method for making 3D reconstructions by serial grinding and imaging, which enables accurate measurement of the morphology of individual ooids within an oolite, as well as the sorting and porosity of a sample. We also provide three case studies that use the morphology of ooids in oolites to extract environmental information. Each case study demonstrates that 2D measurements can be useful if the environmental signal is large relative to the error from 2D measurements. However, 3D measurements substantially improve the accuracy and precision of environmental interpretations. This study focuses on oolites, but errors from 2D measurements are not unique to oolites; this method can be used to extract accurate grain and porosity measurements from any coherent, granular sample.

### 1. Introduction

Ooids are concentrically laminated, sand-sized carbonate grains that are abundant in shallow-water carbonate environments spanning the Archean to the Modern. The prevalence of ooids in carbonate rocks, and the narrow depth range of ooid formation (Eardley, 1938; Geyman et al., 2021; Harris et al., 2019; Newell et al., 1960; Wanless & Dravis, 1989), make ooids a particularly valuable paleoenvironmental proxy and a stable frame of reference for comparing carbonate platforms throughout Earth's history. Carbonate platforms contain many subenvironments such as oolitic shoals, beaches, lagoons, and tidal channels. Each of these settings has unique chemical and physical conditions, which produce ooids with environment-dependent sizes and shapes (Figures 1a and 1b; Mariotti et al., 2018; Trower et al., 2018). Consequently, the morphology of ooids can be used to improve paleoenvironmental reconstructions by refining facies models of ancient carbonate platforms and providing insights into paleohydraulic and geochemical conditions.

While some features of ooid growth remain enigmatic, there is general agreement that ooids grow from the precipitation of calcium carbonate onto a nucleation surface (whether biologically mediated or not), such as a carbonate grain or an existing ooid (Bathurst, 1975). The ooid continues to grow until it is either buried, too big to be transported (Sumner & Grotzinger, 1993), or precipitation and abrasion rates reach a dynamic equilibrium (Figure 1b; Trower et al., 2017). These models provide useful heuristics for understanding the relationship between environmental conditions and ooid size by indicating that increased precipitation rates and more frequent ooid transport lead to larger ooids.

Like size, the shape of the ooid reflects the conditions under which the ooid formed. The shape of an ooid is the result of surface-normal growth from the precipitation of calcium carbonate onto the ooid combined with three types of abrasion: (1) collisional abrasion, which primarily occurs during saltation and produces more spherical shapes, (2) frictional abrasion, which occurs when ooids are rolling and sliding on the

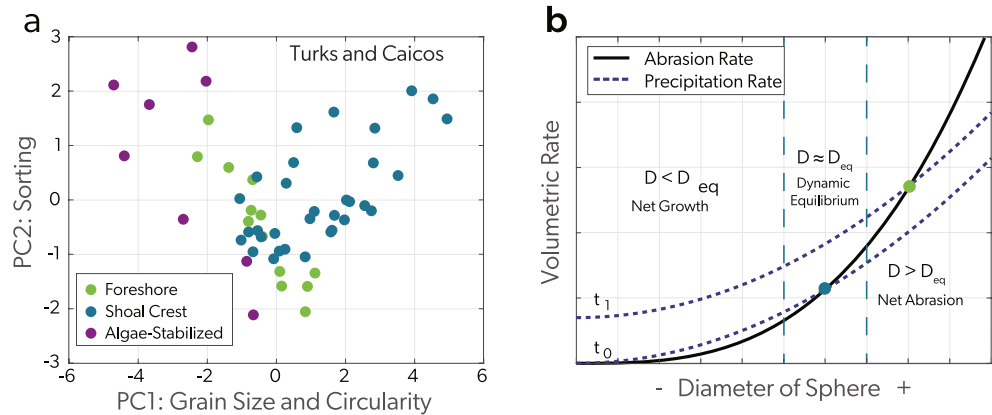


**Figure 1.** (a) Principal component analysis (PCA) of the size and shape of modern ooids from the Turks and Caicos demonstrates that the morphology of ooids is facies dependent (Trower et al., 2018). (b) In a leading model, carbonate saturation state and the hydraulic conditions determine the size of an ooid (Bathurst, 1975; Trower et al., 2017). If the precipitation rate increases (as seen in the upward shift from  $t_0$  to  $t_1$ ), the abrasion rate also will increase and the ooid will reach a new equilibrium size (green dot). Modified from Trower et al. (2017).

substrate, and produces elongated and flattened shapes (Domokos & Gibbons, 2012; Sipos et al., 2018), and (3) fracture, which is the result of collisions with high momentum transfer—typically collisions of large grains at high velocities (Novák-Szabó et al., 2018). An ooid’s concentric laminations preserve the history of its shape as it grows. This growth history may contain information about how sediment transport changes as the grain size and mass increase (Heller et al., 1980). Understanding how the transport mode changes as a function of size can provide clues about the paleohydraulic conditions of ooid-forming environments and perhaps elucidate the formation of giant ooids (>2 mm in diameter), which must have formed under uniquely carbonate-saturated and/or turbulent conditions (Anderson et al., 2020; Heller et al., 1980; Sipos et al., 2018; Sumner & Grotzinger, 1993; Trower, 2020).

Lithified ooids typically have the same composition and physical properties as the binding cement, precluding measurement through physical separation or X-ray computed tomographic techniques. The inability to make 3D measurements has forced researchers to measure the size and shapes of ooids on polished surfaces and in thin sections. Previous research has demonstrated that it is not possible to accurately characterize 3D size and shape distributions from 2D measurements (DeHoff, 1983; Mehra & Maloof, 2018; Mehra et al., 2020). We expand on those results by presenting synthetic experiments with spherical and ellipsoidal shapes, demonstrating that estimates of 3D morphology from measurements made on a 2D cross section are inaccurate and imprecise (Figure 3). To overcome the limitations of 2D measurements, we serially grind, image, and segment oolites using the Grinding, Imaging, and Reconstruction Instrument (GIRI) at Princeton University (Mehra et al., 2020; Mehra & Maloof, 2018), resulting in 3D reconstructions that enable accurate measurement of ooid size and shape.

## 2. The Necessity of 3D Measurements

The limitation of measurements from thin sections and polished slabs is that these measurements represent 2D apparent dimensions instead of 3D grain dimensions. The two central problems with making 2D measurements on 3D objects are the “cut-section effect,” which arises because a grain seldom is cut exactly through its center, and the “intersection probability effect,” because a 2D slice is more likely to intersect a large grain than a small one (Higgins, 2000). These problems can be partially addressed by applying stereological corrections to 2D slices (Higgins, 2000; Kellerhals et al., 1975; Krumbein, 1935; Peterson, 1996; Sahagian & Proussevitch, 1998). However, such solutions require assumptions about several parameters of the sample, including the size distribution type (e.g., log-normal), particle shape, and sorting of the rock

(sorting is measured using a normalized dispersion parameter,  $\sigma^* = \frac{D_{90} - D_{10}}{D_{50}}$ ,  $D_{50}$  is the 50th percentile of the intermediate axis length measurements from a sample). In the case of ooids in an oolite, shape and

sorting are the parameters required to deduce environmental conditions (Figure 1a), so we cannot make these assumptions. Furthermore, these assumptions may not be valid for ooids. For example, ooids within the same layer can be many different shapes, so assuming a single particle shape for stereological analysis would be inappropriate.

As an illustrative example, we quantify the errors associated with 2D measurements by measuring the dimensions of the ellipse formed by the intersection of an ellipsoid and plane. We randomly generate orientations and positions for the intersecting plane and measure the dimensions of the resulting ellipses to simulate a 2D surface formed by cutting through an oolite to make a thin section or polished surface. In Figures 3a–3d, all measurements are from 2D intersections of one ellipsoid (see Figure 2 for the definitions of the morphological measurements).

### 2.1. Size Errors in 2D

Even simple size distributions of spherical and ellipsoidal grains are difficult, if not impossible, to accurately describe from 2D measurements. When using the diameter of spherical grains or the major axis length of ellipsoidal grains (Figure 2), 2D measurements of apparent size underestimate the true size distribution of a granular population (Figures 3a and 3b). For spheres in this experiment, the error is due solely to the cut-section effect. In ellipsoids, the error associated with 2D measurements arises from the cut-section effect as well as intersections that are nearly perpendicular to the major axis, which lead to a misidentification of the major axis (Figure 3c). Similarly, attempts to measure the intermediate axis are complicated by both the cut-section effect and mistaking the minor axis for the intermediate axis when the intersection is nearly perpendicular to the intermediate axis (Figure 3d). Error from 2D measurements of the major axis of an ellipsoid increases as the ellipsoid becomes less spherical, especially as the ellipsoid becomes more prolate (Figure 3e), reaching 35% when the major axis is twice as long as the intermediate axis. For ooids with an aspect ratio similar to the modern oolitic sand on Little Ambergris Cay in the Turks and Caicos Islands (measurements made with Retsch P4 Camsizer in Trower et al., 2018), we expect errors of ~15%, making the  $D_{50}$  of 85% of the samples from Trower et al. (2018) indistinguishable from each other (Figure 3e). Since ooid shape and size are the most heavily weighted variables in PC1 (Figure 1a; Table S1), this error from 2D measurements would make the ooids from these clearly distinct environments indistinguishable, which means the environmental data recorded by ooid morphology is inaccessible. In an attempt to overcome the cut-section effect, it is common practice to measure only ooids that are believed to be cut through the nucleus. Synthetic experiments of this technique demonstrate that, while this method reduces the error if the user properly identifies the nucleus, there are still errors of up to 30% depending on the size of the nucleus and the shape of the ooid (Figure 3f). The reader should note that the experiments in Figure 3 only account for the cut-section effect, and not the intersection-probability effect, so they can be considered minimum-error scenarios.

### 2.2. Shape Errors in 2D

Just as with size, 2D apparent dimensions provide inaccurate approximations of 3D shape. For example, consider a single synthetic ooid with five laminations. All laminations have an aspect ratio  $\left(\frac{b}{a}\right)$  of 0.9, but have a  $\frac{c}{a}$  of 0.5, 0.6, 0.7, 0.8, and 0.9. We randomly slice the ooid 2,500 times, and then measure the aspect ratio of each lamination (Figure 4d). Only including the planes that intersect all five growth bands, the resulting estimate of aspect ratio for a single lamination varies by over 30%, and the percent error of the median measurement is up to 30% (Figure 4e). This error strongly depends on the shape of the growth band, and the error changes from negative to positive as the ooid becomes less oblate and more prolate (Figures 3e and 3d). For comparison, the range of aspect ratios in Turks and Caicos is large (0.70–0.90), but the difference in median aspect ratios between environments is ~10%. For ooids shaped like those from Turks and Caicos, we expect ~20% error from 2D measurements (Figure 3), which would drown out the ~10% environmental signal.

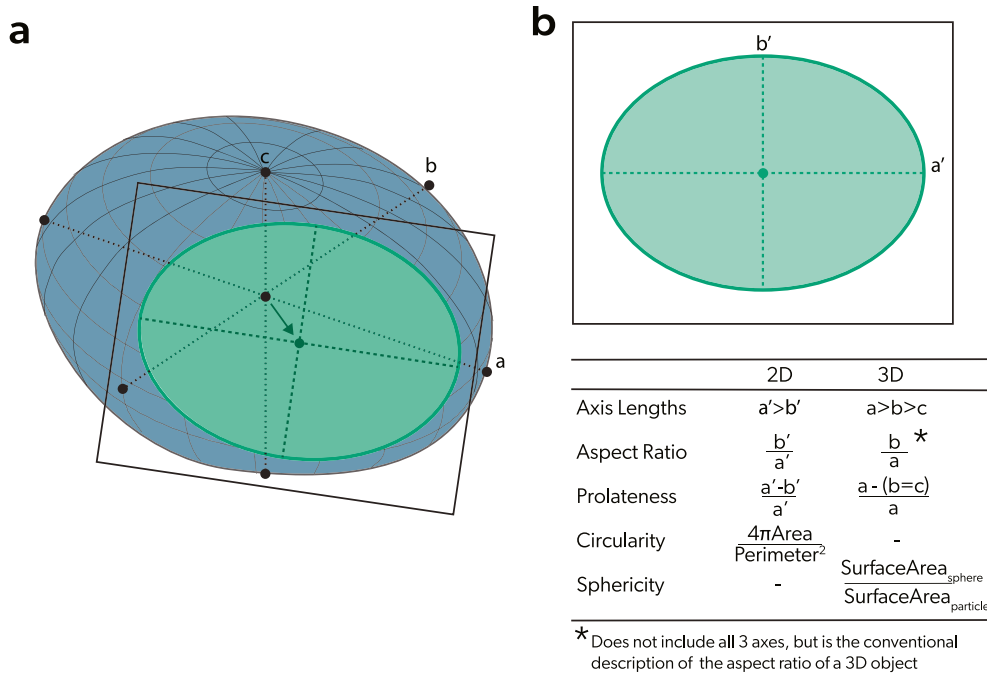


**Figure 2.** (a) An ellipsoid with axes  $a$ ,  $b$ , and  $c$  is cut by a plane, which forms an ellipse with axes  $a'$  and  $b'$ . (b) The resulting ellipse from an ellipsoid cut by a plane is just like an ooid seen in a thin section. The table contains the definitions of common morphological measurements. For sphericity,  $\text{SurfaceArea}_{\text{particle}}$  is the surface area of the particle and  $\text{SurfaceArea}_{\text{sphere}}$  is the surface area of a sphere with the same volume as the particle. We use sphericity instead of aspect ratio because sphericity more completely captures the 3D shape of the ellipsoid (Figure S1). In this manuscript, we measure the surface area of a best-fit ellipsoid to the particle to avoid including small-scale surface roughness in the calculation.

### 2.3. Porosity Errors in 2D

Accurate porosity estimates are crucial for understanding the potential of a rock for both oil extraction and  $\text{CO}_2$  sequestration. Accurate porosity also is vital for modeling interstitial fluid flow, which may be a primary control on early marine diagenesis and chemostratigraphic records (B. Dyer et al., 2017). Just as 2D sections are unreliable recorders of size and shape (Figure 3), individual 2D sections also are unable to accurately describe porosity. For instance, when estimating porosity by measuring the area of every grain and void space on 1,000 random sections through an oolite, any one estimate can be up to 30% wrong (Figure S2). Error will increase when measuring only a subset of grains on each sample (e.g., via point counting). Additionally, while an average of multiple sections can approximate volumetric porosity, a large number of measurements would be required to achieve high accuracy: in the optimistically simple synthetic example, it takes 77 fully segmented slices to be within 5% of the true porosity value for the volume, and 273 slices to be within 1% of the true value (Figure S2).

## 3. Method and Results

### 3.1. Making 3D Measurements

To make direct measurements in 3D, we serially grind and image two oolites using GIRI (Mehra & Maloof, 2018). The first is a lightly cemented oolite associated with eolian coastal dunes from Joulter's Cay, The Bahamas (Halley & Harris, 1979). These oolitic coastal dunes formed  $<1,000$  years before present (Halley & Harris, 1979), and the ooids were sourced from the nearby shoreface. There are 847 images with  $30 \mu\text{m}$  between images (i.e., GIRI step size), and the pixel size in each image is  $5.6 \mu\text{m}$ . The image stack contains over 30,000 ooids, each individually segmented and measured via an image processing pipeline.

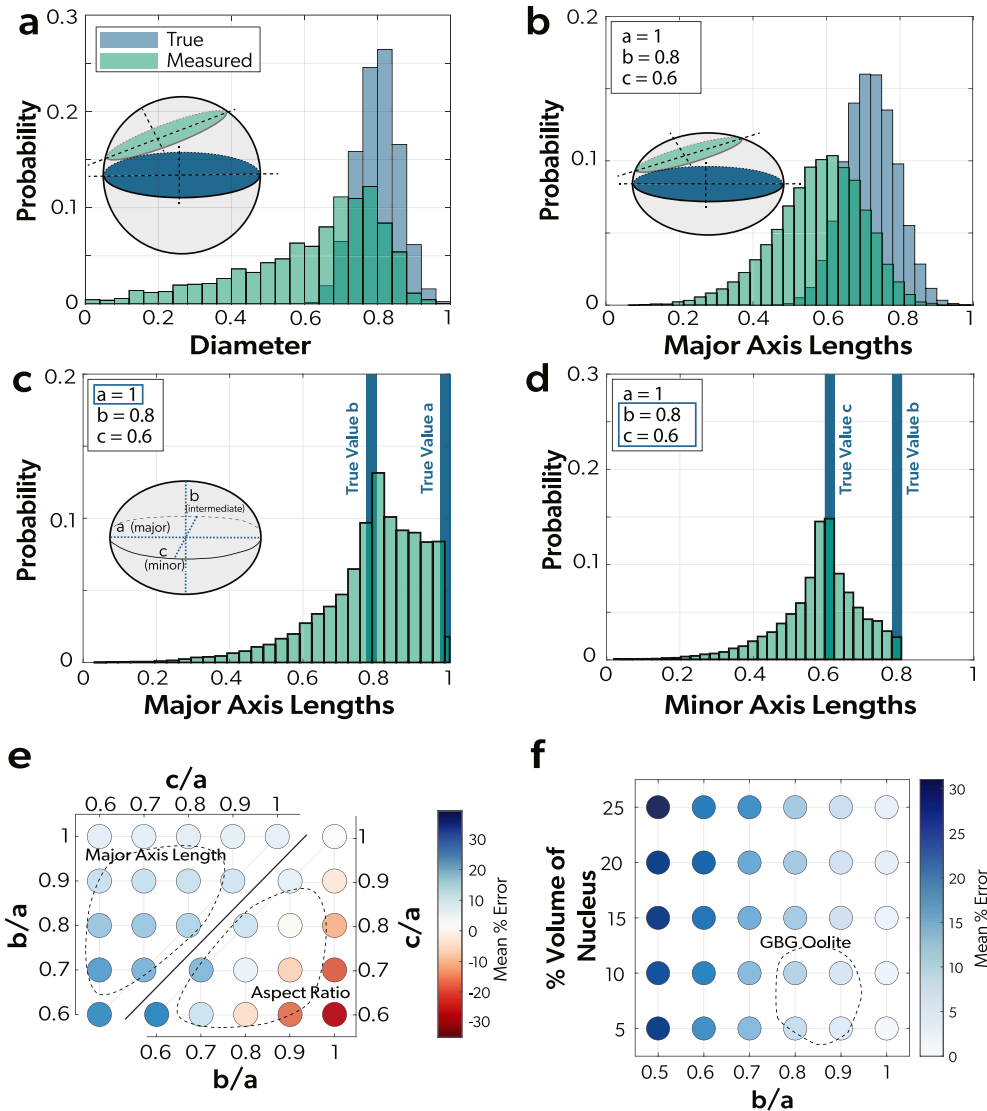


**Figure 3.** (a) The difference between the diameter of a population of spheres and the diameter measured on cut spheres from the same population demonstrates that 2D cuts of a sphere underestimate the true size distribution of the population. (b) The difference between the true major axis length,  $a$ , of a population of ellipsoids and the major axis lengths measured on a random cut through ellipsoids,  $a'$ . (c) Measurement of the major axis of a single ellipsoid on a random 2D slice underestimates the major axis length. (d) Measurement of the minor axis of the ellipse formed by a random intersection with an ellipsoid,  $b'$ , leads to error in the estimation of the intermediate axis,  $b$ . The units for measurements in panels (a–d) are arbitrary and therefore presented as dimensionless. (e) Each dot represents the mean percent error of the median of 100 measurements of the major axis length (top) and aspect ratio (bottom) for a range of ellipsoid shapes. The dashed polygons represent ooids from Joulter's Cay oolinite in Figure 6a. (f) Mean percent error of the median of 100 measurements of the major axis on a plane that intersects the nucleus as a function of aspect ratio and the size of the nucleus. Error increases as the size of the nucleus increases and as the grain becomes less spherical. The ranges of aspect ratios and percent volumes of nuclei in this synthetic example are smaller than the ranges from the Great Salt Lake, which have 25–75th percentile ranges in aspect ratio from  $\sim 0.5$  to 1 and percent of the total ooid volume from  $\sim 1\%$  to 45% (Trower et al., 2020).

The second oolite is from the Early Triassic Great Bank of Guizhou (GBG) in South China. The giant ooids formed on a high-energy platform margin (Lehrmann et al., 2012). The image stack contains 2,259 images with  $20\ \mu\text{m}$  between images, the pixel size is  $5.6\ \mu\text{m}$ , and there are 478 ooids in the sample. The space between images is smaller in this sample to allow the reconstruction of more detailed ooid growth histories (Section 4.3). For complete details of the grinding and imaging routines, see Mehra and Maloof (2018).

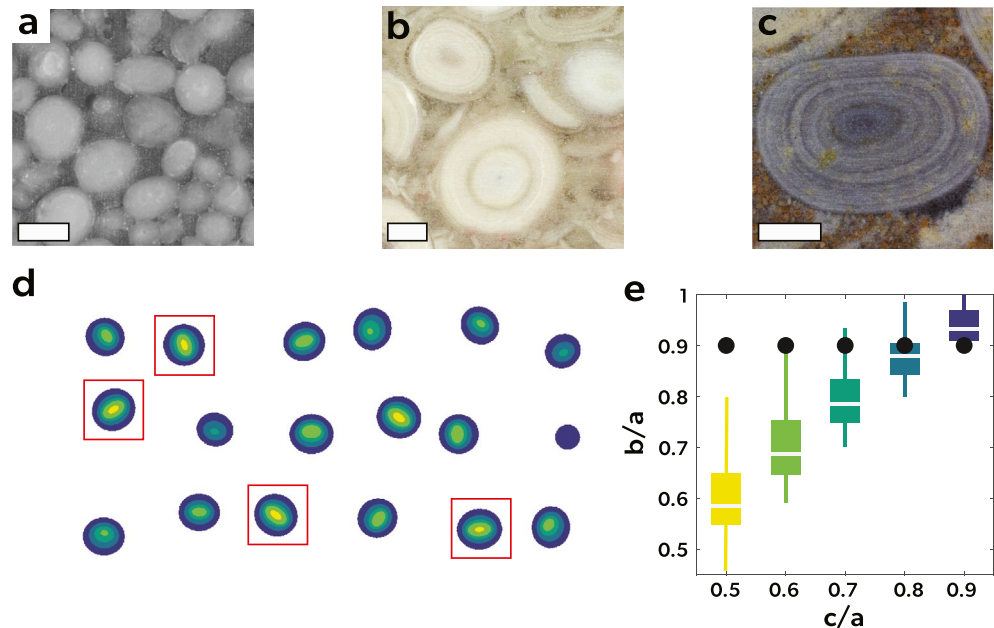


**Figure 4.** (a) Holocene oolite from Joulter's Cay, The Bahamas. White scale bar is 100  $\mu\text{m}$ . (b) Giant ooids from the Great Bank of Guizhou in South China (Lehrmann et al., 2012). White scale bar is 1 mm. (c) Giant ooids from the Etina Formation in Australia. White scale bar is 5 mm (Rose et al., 2013). (a–c) These photographs demonstrate the difficulty of identifying the nucleus of an ooid from a 2D slice through an oolite. In (a), there are no clear nuclei in any of the ooids, in (b and c), banding of the ooids make it appear as if the cut is through the nucleus even though our 3D models reveal that the ooids in these images are not sliced through their nuclei. (d) 18 of the 2,500 random cuts through a synthetic ellipsoidal ooid with five laminations show the many different cross sections that can be produced from slicing a single ellipsoid. The red boxes outline slices that intersect all five laminations. (e) The box plot shows the distribution of apparent aspect ratio values produced from 2D slices of the ooid in (d), and only slices that intersect the nucleus are used to calculate these distributions. From left to right in (e), the error of the median aspect ratio is  $-31\%$ ,  $-21\%$ ,  $-11\%$ ,  $-2\%$ , and  $+3.2\%$ . The colors of the box plots match the colors of the laminations in (d). Black dots mark the true aspect ratio value for the laminations. The axis ratios used are within the range measured from Joulter's Cay (Figure 6a).

### 3.2. Image Processing

Segmenting and measuring 3D granular particles is a challenging task and an active field of research in computer vision, material sciences, and biology (Jaquet et al., 2013). The challenge is in accurately separating objects of the same material that are connected as a result of packing and/or growing together (like ooids cemented by calcium carbonate). The first step of segmentation is to identify the ooid and non-ooid pixels in an image, for which we use a convolutional neural network (CNN). We built a training data set by manually tracing over pixels of the ooid and of the non-ooid class pixels (Figure 5b). For both samples, these training pixels were distributed across 10 different images dispersed throughout the image stack. We then used these data to train a CNN with two local and one global layers, each connected to associated ReLU and max pooling layers (Figure S3). Next, we applied the trained network to each image in the stack, producing completely classified images (Figure 5c). To separate and individually label each ooid, the classified images were loaded into Avizo (a scientific visualization software package), which gave each slice a thickness corresponding to the grinding step size, resulting in volumetric pixels (voxels). As subsequent operations were optimized for isotropic voxels, the data were interpolated so that the resolutions for all three dimensions were the same (the final voxels for the Joulter's Cay oolite are  $10 \times 10 \times 10 \mu\text{m}$ , and the final voxels for the GBG oolite are  $40 \times 40 \times 40 \mu\text{m}$ ). This technique is common practice in 3D imaging techniques like X-ray computed tomography (Capowiez et al., 2003; Pierret et al., 2002). We applied a series of morphological operations, including openings and closings to the image stack to remove spurious small, incorrectly classified regions from the data set. Next, to isolate individual ooids, we implemented a modified watershed transform, which includes (1) finding the distance of every ooid-labeled pixel to the nearest non-ooid label-

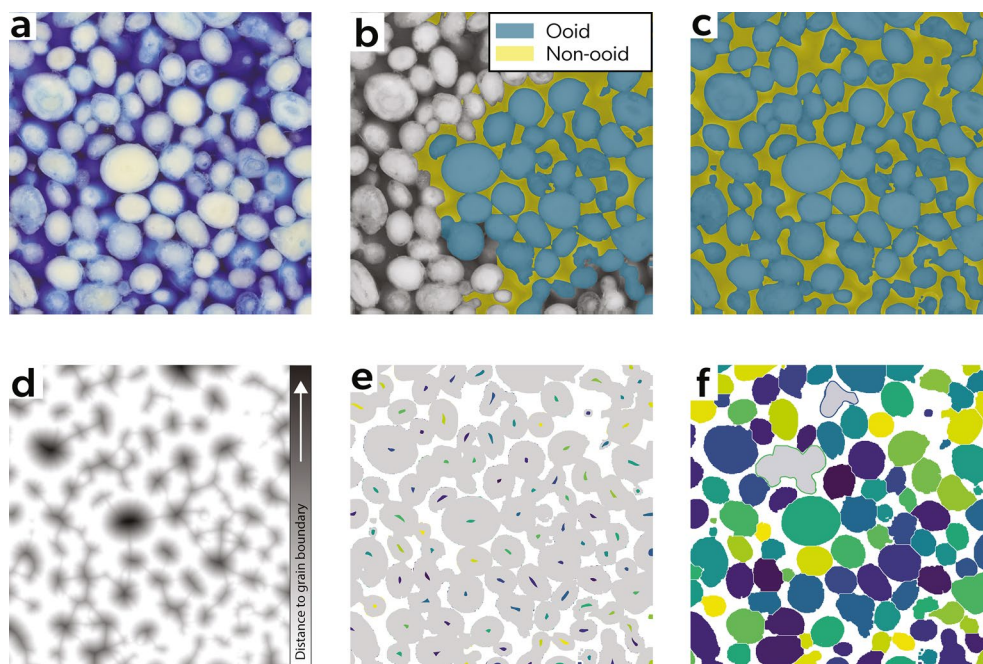


**Figure 5.** (a) An example image from the Joulter's Cay eolianite. (b) We create a training mask by tracing over an image, which then is used to train a convolutional neural network (CNN). (c) An image classified by the CNN. (d) The euclidean distance of each ooid-labeled pixel from the nearest non-ooid pixel. Darker color means the distance is greater. (e) We filtered out local distance maxima by using the extended-maxima transform (colored dots) to seed the watershed, and masked out the rest of the ooid pixels (gray). (f) After the watershed transform, all ooids are individually labeled and ready for measurement. All particles with a major axis length shorter than  $100\ \mu\text{m}$  or longer than  $750\ \mu\text{m}$  were removed to filter out non-ooid particles like shells and grapestones (grayed out ooids).

led pixel, (2) using the regional maximum distance as the “seeds” for the watershed, and (3) assigning each ooid pixel to one of the “seeds” based on the distances from step 1 (Figures 5d–5f). Ooid size measurements were made on each individual ooid in MATLAB using the built in regionprops3 function, which provides measurements including principal axis lengths, volume, centroid location, and surface area. From these measurements, it is possible to derive shape and sorting metrics (Figure 6). Complete MATLAB code for the CNN and the specifications for the watershed in Avizo are provided in the data repository (<https://doi.org/10.34770/4yys-g270>) along with the images and 3D models.

The process of grinding and imaging is completely automated (Mehra & Maloof, 2018), and the time required depends on the size of the sample; for a hand-sized sample, it takes  $\sim 1.5$  h of machine time per mm of thickness. Building a training data set takes  $\sim 3$ –4 person hours. Training the neural network and segmenting the images requires 12–24 machine hours (depending on the size of the sample), then eight person hours for any necessary post-processing. It also is possible to simultaneously grind and image multiple samples, as many as twenty samples the size of a standard thin section ( $24 \times 46$  mm) can fit on GIRI at one time. If the samples were 40 mm thick, it would take  $\sim 168$  unsupervised machine hours to grind and image all the samples. Depending on the similarity of the samples, it is even possible to avoid training a new model, which would again reduce the total analysis time.

#### 4. Discussion

Environmental conditions are imparted on ooid morphology through the physics and chemistry of sediment transport and  $\text{CaCO}_3$  precipitation. Both of these processes are complex and nonlinear, which introduce noise to the environmental signal. Despite this noise, empirical studies have found that ooid size and shape can reflect the conditions under which the ooids formed (Heller et al., 1980; Mariotti et al., 2018; Trower et al., 2017, 2018). Here, we will discuss three important applications of ooid morphology to the study of Earth's history, and how 3D measurements increase the utility of ooids as a tool for understanding the past.

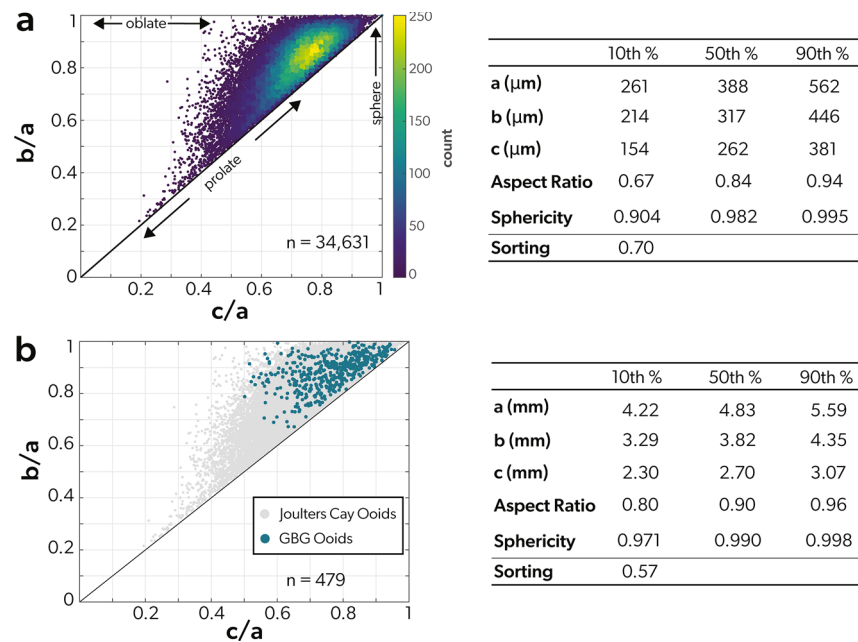


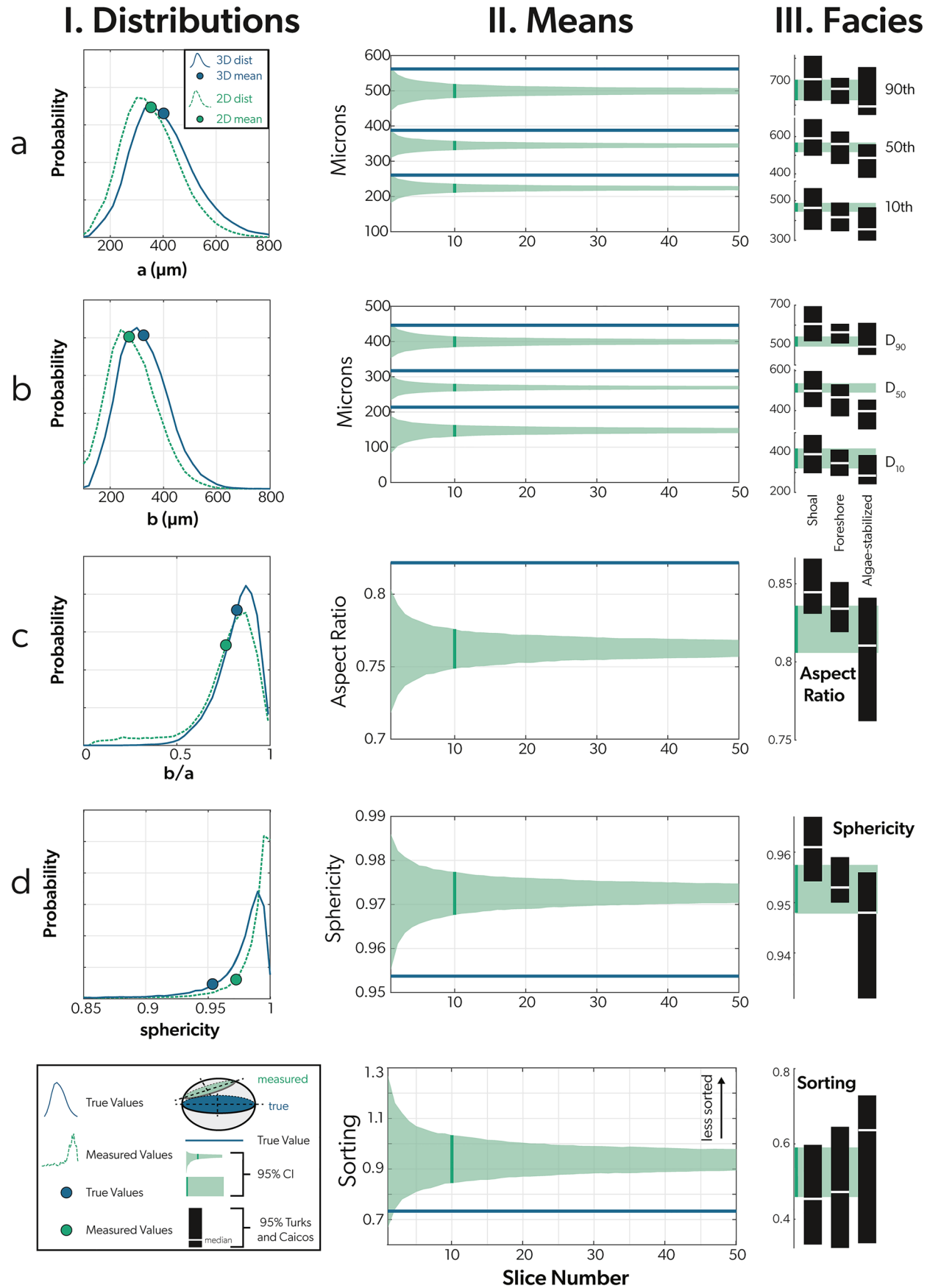
**Figure 6.** Grain size and shape measurements from 3D reconstructions. (a) Holocene oolite from Joulter's Cay, Andros Island, The Bahamas, and a table of measured values. (b) Triassic oolite from the Great Bank of Guizhou, China, and a table of measured values. The values only represent ooid grains, and do not include the many fragments and other grains in the sample.

#### 4.1. Distinguishing Environments

In many ways, an eolian-sorted oolite, like the one from Joulter's Cay (Figure 6), is an ideal rock to study in 2D. In the sample from Joulter's Cay, the ooids are a similar shape and there is a narrow size range (sorting = 0.70), which together limit the error in two-dimensional measurements of grain size (Higgins, 2000). Yet, even in this nearly ideal sample, the inaccuracy of 2D measurements of ooid size and shape limits their utility as paleoenvironmental indicators.

To demonstrate how 2D measurements of the sample from Joulter's Cay would have incorrectly characterized the size of these ooids, we measured the apparent size and shape of the ooids from each image in the GIRI image stack and compared these 2D measurements to the true 3D values. We only included ooids cut within 30  $\mu\text{m}$  of their centroid—known from the 3D reconstruction—in order to simulate a user identifying ooid centers in a thin section. As predicted by the synthetic experiments in Figure 3, the 2D measurements underestimate the true size of the major and intermediate axes of the ooid (Figures 7Ia, 7Ib). Additionally, the 2D apparent sizes from any given slice vary by up to 10%. The cumulative mean of many slices does eventually converge, but the 2D mean is inaccurate by up to 20% (Figures 7IIa, 7IIa).

Two-dimensional measurements of the shape and sorting of ooids in the Joulter's Cay oolite also produce incorrect values (Figures 7Ic, 7Id). Errors in the estimates of aspect ratios are complex (Figure 3e), but on average, the 2D measurements underestimate the aspect ratio. Two-dimensional measurements also underestimate the sorting, but overestimate the sphericity. Just as with size, the shape and sorting values vary from slice-to-slice and the cumulative mean of many slices converges to an incorrect mean value (Figures 7IIc, 7IIc). In the case of the Joulter's Cay sample, the inaccuracy of the sorting estimate from 2D is important because, with reduced context (e.g., poor outcrop exposure or core from a borehole) the paleoenvironmental interpretation of the sample would change. For example, because of the efficiency with which wind sorts sediment, we expect the lithified eolianite to show improved sorting compared to the source shoreface; this pattern is observed in the 3D data: the Joulter's Cay sample has a sorting of 0.70, which is better sorted than all but one of the 23 ooid samples from a 1 km transect of the nearby shoreface (which have a 10–90th percentile of 0.81–2.5), and is 48% better sorted than the average shoreface ooid sample on the northern part of Andros Island (Figure S4). But the mean sorting estimate from 200 slices, which under-



estimates the true sorting by 27% (Figure 7Iie), would make the sorting of the eolianite indistinguishable from the nearby shoreface.

Since 2D measurements cannot accurately determine the absolute size and shape of ooids, models that utilize absolute measurements of morphology require 3D measurements. However, if a model only requires distinguishing relative differences between samples, 2D measurements can be appropriate if the difference between environments is large relative to the noise from 2D measurements. A comparison between the size of the 95% confidence interval of a 2D measurement from 10 slices (equivalent in area to a standard thin section) in the Joulter's Cay image stack and the difference in the medians of the environments from Turks and Caicos can provide intuition for when 2D measurements are able to distinguish between environments (Figure 7III). The ooids from Turks and Caicos were measured with a camsizer (Trower et al., 2018), which makes quasi-3D measurements by measuring the projection of a grain. Non-ooid grains were removed from both the Turks and Caicos and Joulter's Cay datasets by filtering out shells and grapestones. There are two main takeaways from this comparison. First, the imprecision from 2D measurements relative to the difference between environments is smaller in measurements of axis lengths (particularly intermediate axis length) than measurements of shape and sorting (Figure 7III). Second, if the difference between environments is large, it may be possible to distinguish between them despite the imprecision of 2D measurements. For example, the difference in ooid morphology between the shoal and foreshore would be too small to distinguish from 2D measurements of any metric. However, it might be possible to distinguish the algae-stabilized ooids from the other environments based on the shape and intermediate axis measurements because the morphological differences between the environments are large relative to the uncertainty from 2D measurements. An ooid grainstone could represent any number of different paleoenvironments, and while ooid morphology is not the only proxy for distinguishing between these paleoenvironments, ooid morphology is a rich source of environmental data. For example, accurately mapping the differences in ooid morphology on a platform could reveal important sedimentological and geochemical information such as transport direction on a platform or  $\Omega_{\text{Aragonite}}$  gradients.

#### 4.2. Effect of 2D Measurements on Modeling Aragonite Saturation

There is a long history of using ooids to infer the chemistry of ancient oceans (Opdyke & Wilkinson, 1990; Sandberg, 1983; Wilkinson & Given, 1986). One recent study leveraged the fact that ooid size reflects a dynamic equilibrium between precipitation rate and abrasion rate to use the size of giant ooids to infer the saturation state of  $\text{CaCO}_3$  ( $\Omega$ ), temperature,  $\text{pCO}_2$ , and seawater alkalinity (Trower, 2020). This study determined that the formation of giant ooids required  $\Omega_{\text{Aragonite}}$  2–5x greater than modern ooid-forming environments, depending on the size of the ooid and the temperature of the water (Trower, 2020). Similarly, Li et al. (2020) applied this model to giant ooids from the Triassic of south China, including one sample from the GBG. Li et al. (2020) concluded that  $\Omega_{\text{Aragonite}}$  ( $\Omega_A$ ) likely was greater than 7, and accompanied by DIC and seawater alkalinity twice the modern values, and pH lower than the modern value. This model has several tunable parameters and it is not our intention to evaluate the veracity of the model. Instead, we demonstrate the sensitivity of the output from models like this one to uncertainties in ooid morphology by comparing the predicted  $\Omega_A$  for 2D and 3D data (Note: Ooid morphology is the only input to this model that can be measured directly).

**Figure 7.** A comparison of 2D and 3D measurements of ooid morphology. The 2D measurements were made by measuring the dimensions of ooids in every photograph from the Grinding, Imaging, and Reconstruction Instrument (GIRI) data set. Only ooids cut within 30  $\mu\text{m}$  of their center are included in the data set to simulate researchers only including ooids cut through the nucleus. This choice reflects a small nucleus compared to examples from the Great Salt Lake (Trower et al., 2020), and should be considered a minimum-error scenario. Sphericity of the 2D ooids is calculated by assuming the ooids are perfectly prolate and then using the equation for 3D sphericity (Figure 2). (Column I) A comparison of the distribution of 2D and 3D measurements. (Column II) We shuffled the slices from the GIRI image stack 2,000 times, then calculated the cumulative mean in each shuffled stack. The cumulative mean of many slices converges on measurements that underestimate the size, aspect ratio, and sorting, but overestimate the sphericity. Each slice contains  $\sim 400$  ooids, and is 1/10th the surface area of a standard thin section, so every 10 slices is equivalent to measuring every ooid in a thin section. A dark green vertical bar marks the tenth slice. (Column III) A comparison of the uncertainty from 2D measurements of the Joulter's Cay sample to the size and shape of ooids from different facies on Little Ambergris Cay, Turks and Caicos (Trower et al., 2018). The width of the light green bar represents the uncertainty of the cumulative mean of 10 slices; the position of the bar has been adjusted to easily compare the uncertainty in 2D measurements to the environmental variance. If the medians from Turks and Caicos are within the light green bar, they would be indistinguishable based on 2D measurements.

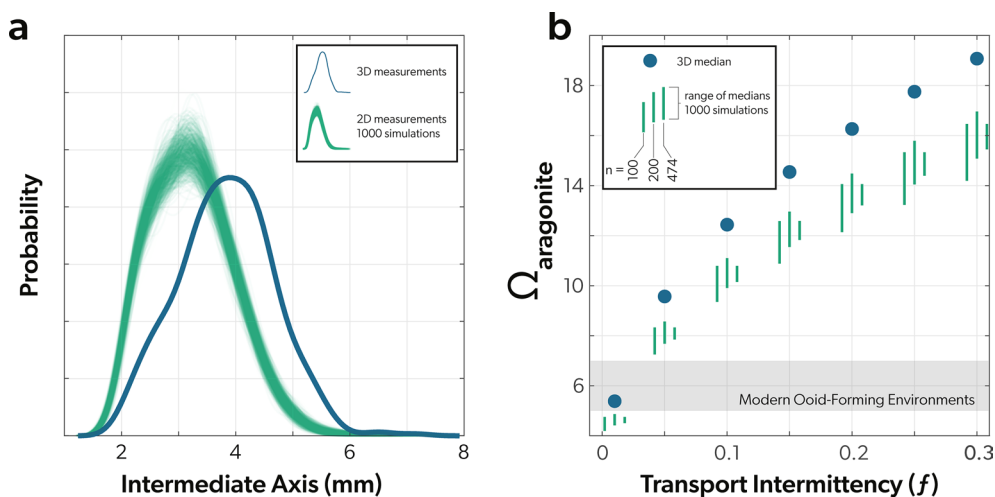


**Figure 8.** (a) The distribution of intermediate axis lengths of all ooids in the Great Bank of Guizhou (GBG) oolite measured in 3D compared to the distributions of the minor axes of all ooids in the GBG oolite measured on a randomly oriented 2D plane. To simulate user identification of the nucleus, only ooids cut within 600  $\mu\text{m}$  of the centroid were included. (b) The predicted median  $\Omega_A$  calculated from the 3D intermediate axis lengths compared to the median 2D minor axis lengths from the simulations in (a). We also calculated the median of random samples of 100 and 200 ooids from the GBG oolite to demonstrate how smaller sample sizes lead to even less accuracy and precision.

To calculate the predicted  $\Omega_A$  for the Early Triassic ooids from the GBG, we used the parameters for Triassic seawater and transport intermittency ( $f$ ) values of 0.01–0.3 (meaning grains are in active transport 1%–30% of the time) as defined by Li et al. (2020). To simulate measuring ooids in 2D, we cut each of the 474 ooids from the GBG oolite with a randomly oriented plane. We required that the cut pass within 600  $\mu\text{m}$  of the nucleus (the median radius of the nucleus based on measurements of 3D tracings of the nuclei) and only included ooids larger than 2 mm (the minimum size for a giant ooid), and repeated this experiment 1,000 times (Figure 8a). The median intermediate axis length from 3D measurements is 3.8 mm, while measurements from 2D slices estimate a median intermediate axis length of 3.1–3.2 mm. This discrepancy represents 16%–18% error, similar to the prediction for this shape and nucleus size in Figure 3f. Figure 3f also suggests that the error and uncertainty from 2D measurements of less spherical ooids with larger or no identifiable nuclei (like giant ooids from the Etina Formation of Australia shown in Figure 4c) would be much larger. The 16%–18% error from 2D measurements propagates through the model and leads to an underestimate of  $\Omega_A$ . When all 474 ooids are measured, 2D measurements result in errors of 11.7%–16.3% when  $f = 0.01$ , and errors increase to 13.7%–19.0% when  $f = 0.3$ . When only a subsample of the ooids are measured, the error can increase to 25.6% and the results become less precise (Figure 8b). The error and imprecision suggest that 2D measurements are able to distinguish large changes in  $\Omega_A$ , like the difference between modern and Early Triassic ooid-forming environments, but the accuracy and precision of 3D reconstructions likely would be required to decipher environmental differences across time and space on an individual platform like the GBG, or between time periods like the Neoproterozoic and Early Triassic. Additionally, the reader should note that the model is very sensitive to the transport intermittency value. For example, if the intermittency value were 0.01, which is the value used in Trower (2020) and within the range explored in Li et al. (2020), the Early Triassic  $\Omega_A$  would be indistinguishable from modern ooid-forming environments (Figure 8b; Li et al., 2020).

### 4.3. The Growth History of Giant Ooids

Previous studies have outlined a method for reconstructing paleohydraulic conditions from the growth histories of ooids (Heller et al., 1980; Sipos et al., 2018; Trower et al., 2020). In a recent study of ooids in the Great Salt Lake, Trower et al. (2020) presented an innovative methodology for quantitatively describing ooid growth histories and determining the relative amount of growth and abrasion time during the formation of each lamination. This technique is possible because of the development of a geometric model for how the

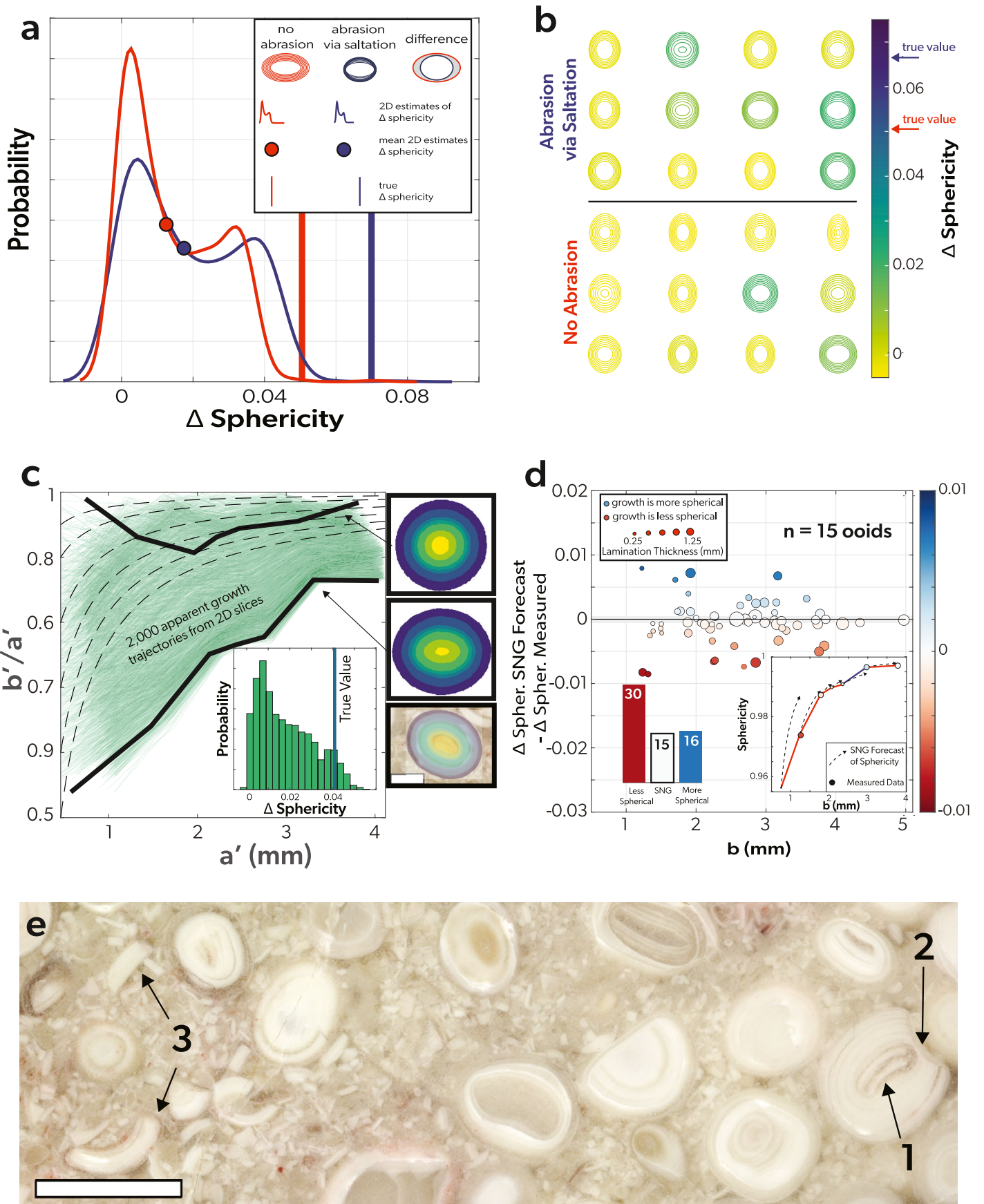
shape of an ooid evolves as it forms (Sipos et al., 2018; Trower et al., 2020). As described in this shape evolution framework, the precipitation of calcium carbonate onto an ooid is modeled as surface-normal growth (SNG), which causes the ooid to become more spherical at a given rate (red in Figure 9a). The change in shape resulting from abrasion depends on whether the ooid is transported via saltation, or by rolling and sliding. Collisional abrasion associated with saltation causes ooids to become spherical more rapidly than SNG predicts, which has been verified by studies of modern ooids in the Turks and Caicos and the Great Salt Lake (Trower et al., 2018, 2020). Frictional abrasion from rolling causes ooids to become more elongate (Domokos & Gibbons, 2012; Sipos et al., 2018).

This geometric model provides a tool for using the shape evolution of ooids as they grow to interpret the hydraulic conditions under which the ooids formed. However, the effect of ooid growth history on shape is small compared to the uncertainty introduced by 2D measurements. Consider two ooids with identical nuclei; one ooid grew in the complete absence of any abrasion, while the other experienced substantial collisional abrasion throughout its formation. The change in sphericity ( $\Delta$  sphericity) over the entire growth history of these two ooids differs by only 0.015, while the uncertainty from 2D measurements (0.065) is over four times the size of this environmental signal (Figure 9a). We only included cuts that intersected some portion of the nuclei, so the inaccuracy and imprecision is the result of different orientations of the 2D intersection producing many different apparent growth histories for the same ooid (Figure 9b). For modern unlithified ooids, like those from the Great Salt Lake, it is possible to verify sample orientation through careful sample preparation and to avoid some of this error from unknown orientations (Trower et al., 2020), but this preparation is not possible with lithified ooids.

Extending the application of the geometric model of ooid growth into the stratigraphic record requires three-dimensional reconstructions of ooids and the laminations recording their growth history. With serial sections from GIRI, we are able to reconstruct growth histories in three dimensions by tracing a single lamination on dozens of slices. From these traces, we build a 3D model of the cortex and measure the dimensions of an ooid as it grows. We model the expected shape evolution from SNG in the absence of abrasion, and attribute deviations from this growth model to abrasion. We apply this 3D method to the giant ooids from GBG to demonstrate both the necessity of 3D measurements, and how 3D measurements can provide new insights into the formation of giant ooids.

By measuring the aspect ratio of each growth band on a randomly oriented plane intersecting the 3D reconstruction of a single ooid from the GBG sample, we simulate the apparent growth history of one of these giant ooids as recorded by 2D intersections. Like in the synthetic example, we find that 2D growth histories of the same ooid can show an alarming range of growth histories, including a few that suggest a decrease in the aspect ratio despite the 3D reconstruction showing this ooid became much more spherical as it grew (Figure 9c). If we assume the ooid from the 2D intersection is prolate (ooids tend to be more prolate than oblate; Figures 6a and 6b) and then calculate the change in sphericity as it grows, we find that, like in Figure 9a, the 2D growth histories underestimate the change in sphericity (Figure 9c inset). This experiment only includes planes that cut through the nucleus and these ooids have high sphericities relative to the ooids from Joulter's Cay and other giant ooids like those from the Etina Formation (Figure 4c), so this result is a minimum-error scenario. This error means that analysis of growth histories using 2D intersections would underestimate processes that make ooids more spherical (i.e., surface-normal precipitation and saltation) when trying to understand the environments that made giant ooids.

Using the 3D data, we found that, as the giant ooids grew, they tend toward a more spherical shape. However, in most cases, the sphericity increases more slowly than predicted by SNG (Figure 9d). Collisional abrasion as grains saltate causes the grains to become spherical more rapidly than predicted by SNG (Sipos et al., 2018; Trower et al., 2018), so the slowed increase in sphericity probably is the result of frictional abrasion from transport in contact with the seafloor. While there is evidence for collisional abrasion, the predominance of frictional abrasion suggests that the primary mode of transport occurs between the threshold for motion and the threshold for saltation (Novák-Szabó et al., 2018). In many cases, the  $\Delta$  sphericity is very close to that predicted by SNG, which could be the result of infrequent transport or growth in the sediment pile (*sensu* Anderson et al., 2020). Laboratory and natural experiments have shown that when the particle size is large, frictional abrasion dominates at low velocities, and at high velocities fragmentation occurs, instead of the chipping that occurs in smaller particles (see Figure 7 in Novák-Szabó et al. (2018)). These same



experiments suggest that, for sufficiently large particles, the threshold for saltation is effectively the same as the threshold for fragmentation. Since there is abundant evidence of fragmentation in the GBG oolite (Figure 9e), we can infer that water velocities occasionally reached the saltation threshold. If we assume a minimum Rouse number of 2.5 (representing the threshold of bed load transport), we determine that to cause fragmentation, bed-shear velocity must have reached at least  $\sim 45$  cm/s. There are not many measurements of bed-shear velocity in ooid-forming environments, but for reference  $\sim 45$  cm/s is over an order of magnitude higher than bed-shear velocity predicted for oolitic sands from Joulter's Cay and Lee Stocking Island, The Bahamas (Prager et al., 1996), and roughly in the range of bed-shear velocities that form sand-to-gravel waves in the West Solent tidal channel in England (Dyer, 1972) and bed-shear velocities associated with winter storms measured in the shoals of the northern Gulf of Mexico (Siadatmousavi & Jose, 2015).

The bed-shear velocity associated with fragmentation cannot be the typical environmental condition that the giant ooids formed in because consistent fragmentation associated with high bed-shear velocities would not allow ooids to grow this large. Instead, the presence of fragments suggests that the ooids grew to their large size under calmer conditions (i.e., bed-shear velocities below the threshold for saltation of the giant ooids), but were occasionally exposed to bed-shear velocities high enough to cause fragmentation. Several scenarios exist that could explain both the size of the ooids and the occurrence of fragmentation including (1) the giant ooids grew in a calmer environment and were transported to a higher-energy environment, (2) ooids grew within the sediment pile causing ooids to be oversized (Anderson et al., 2020), or (3) the ooids predominantly grew on the seafloor under calmer conditions where the dominant processes were surface normal growth and frictional abrasion from rolling, but occasional storms led to high bed-shear velocities and fragmentation. Option one fails to explain why there are laminations on large, fragmented ooid cortices (Figure 9e). Conversely, options two and three are able to explain this re-coating of large ooid fragments by suggesting that occasional storms cause the fragmentation of many of the giant ooids, followed by calmer conditions (or burial) permitting the continued growth of giant ooids. Distinguishing between options 2 and 3 is difficult. We may expect that ooid growth in the sediment pile would lead to more oblate shapes due to the weight of overlying sediment and the anisotropy of fluid flow due to sediment layering, similar to the formation of siderite concretions, which tend to be oblate (Fisher et al., 1998). The 3D reconstruction of the GBG oolite shows that these ooids tend to be more prolate than oblate (Figure 6), which is consistent with rolling, but it is possible that the oblateness from forming in the sediment pile was removed by abrasion during subsequent transport. Anderson et al. (2020) also suggest that if giant ooids are growing in the sediment pile, there may be discontinuities on each growth band representing grain-to-grain contacts. However, Anderson et al. (2020) recognize that these discontinuities rarely are seen because the ratio of the total surface area of a sphere to the area of grain-to-grain contacts is very small, and there is a low probability that any cross-sectional cut would intersect the points of contact. Grinding and imaging giant ooids with a small step size (5–10  $\mu\text{m}$  between images) could allow the identification and mapping of these discontinuities and grain-to-grain contacts in 3D to determine if growth within the sediment pile could be partly responsible for the growth of giant ooids.

## 5. Conclusions

Many studies have argued that ooid size and shape are related to environmental conditions. This link between morphology and environment has been modeled both numerically and physically (Sipos et al., 2018; Sumner & Grotzinger, 1993; Trower et al., 2017), and is observed in modern environments (Trower

**Figure 9.** (a) A comparison of the  $\Delta$  sphericity from two end-member ooid growth histories. The red represents an ooid grown in the complete absence of abrasion. The blue is an ooid that experienced intense collisional abrasion (the grain-averaged abrasion increment at each time step was 70% of the growth increment Trower et al., 2020). Measurements of sphericity from the 2D slices assume that the ooid is prolate. (b) A catalog of random 2D intersections of the ooids shown in (a), colored by the apparent  $\Delta$  sphericity. Red and blue arrows depict the location of the true values from (a). (c) The green lines are 2,000 simulated growth paths of an ooid if the aspect ratio is measured on 2D intersections. The solid black lines are the growth histories from cuts of the ooid displayed to the right. (c-inset) The  $\Delta$  sphericity of the ooid from the first growth band to the last growth band. The histogram depicts the  $\Delta$  sphericity of all apparent growth paths from (c), and assumes the ooid is prolate (as opposed to oblate). For reference, the sphericity of a sphere is 1.0 and the sphericity of a cube is 0.806. The true value line is made from the 3D reconstruction. (d) The difference between the forecasted surface normal growth (SNG)  $\Delta$  sphericity and the measured  $\Delta$  sphericity as a function of intermediate axis length. At all sizes measured, ooids predominately become less spherical than predicted by SNG. (d-inset) The sphericity of one ooid as it grows measured in 3D compared to the predicted sphericity from SNG. (e) Oolite with giant ooids from Great Bank of Guizhou. (1) fragment of giant ooid is the nucleus for a different giant ooid, (2) Abrasion/fracture surface on giant ooid overgrown by calcium carbonate, and (3) giant ooid fragments in the matrix of the oolite. Scale bar is 2 mm.

et al., 2018, 2020). Ooid morphology has the potential to be a powerful tool for interpreting the rock record, but the error associated with 2D measurements drowns out many of the environmental signals, severely limiting its application to the stratigraphic record. By measuring ooid morphology in 3D, we can begin to sharpen our interpretations of the ancient rock record, and fully utilize the potential of ooids as environmental indicators. Furthermore, errors introduced from 2D measurement of grain size and shape are not unique to ooids. Future work on everything from grain size and porosity of sandstones to the composition of igneous and metamorphic rocks will benefit from the more accurate data offered by 3D measurements.

## Data Availability Statement

All original images and the models are available at Princeton Dataspace: <https://doi.org/10.34770/4yys-g270>. The code used for image segmentation and to process the data is located at <https://doi.org/10.5281/zenodo.4516560>.

## Acknowledgments

This study benefited from feedback by E. Geyman and R. Manzuk. We thank D. Lehrmann and J. Payne for providing the sample from the Great Guizhou Bank. S. Ravi and I. Buynevich generously allowed us to use their laser particle analyzer and camsizer, respectively. G. Lobet and E. Cano assisted with lab work. The authors would like to thank E. Trower, G. Rankey, and D. Buscombe for their helpful comments. This work was supported by NSF Earth Sciences Grant 1028768 to A. Maloof and Princeton University.

## References

- Anderson, N. T., Cowan, C. A., & Bergmann, K. D. (2020). A case for the growth of ancient ooids within the sediment pile. *Journal of Sedimentary Research*, 90(8), 843–854.
- Bathurst, R. G. C. (1975). *Carbonate sediments and their diagenesis*. Amsterdam, The Netherlands: Elsevier.
- Capowiez, Y., Pierret, A., & Moran, C. J. (2003). Characterisation of the three-dimensional structure of earthworm burrow systems using image analysis and mathematical morphology. *Biology and Fertility of Soils*, 38(5), 301–310.
- DeHoff, R. (1983). Quantitative serial sectioning analysis: Preview. *Journal of Microscopy*, 131(3), 259–263.
- Domokos, G., & Gibbons, G. (2012). The evolution of pebble size and shape in space and time. *Proceedings of The Royal Society A Mathematical Physical and Engineering Sciences*, 468, rspa20110562.
- Dyer, B., Higgins, J. A., & Maloof, A. C. (2017). A probabilistic analysis of meteorically altered  $\delta^{13}\text{C}$  chemostratigraphy from Late Paleozoic Ice Age carbonate platforms. *Geology*, 45(2), 135–138.
- Dyer, K. (1972). Bed shear stresses and the sedimentation of sandy gravels. *Marine Geology*, 13(2), M31–M36.
- Eardley, A. J. (1938). Sediments of Great Salt Lake, Utah. *AAPG Bulletin*, 22(10), 1305–1411.
- Fisher, Q., Raiswell, R., & Marshall, J. (1998). Siderite concretions from nonmarine shales (Westphalian A) of the Pennines, England; controls on their growth and composition. *Journal of Sedimentary Research*, 68(5), 1034–1045.
- Geyman, E. C., Maloof, A. C., & Dyer, B. (2021). How is sea level change encoded in carbonate stratigraphy? *Earth and Planetary Science Letters*, 560, 116790.
- Halley, R. B., & Harris, P. M. (1979). Fresh-water cementation of a 1,000-year-old oolite. *Journal of Sedimentary Research*, 49(3), 969–987.
- Harris, P., Diaz, M. R., & Eberli, G. P. (2019). The formation and distribution of modern ooids on Great Bahama Bank. *Annual Review of Marine Science*, 11, 491–516.
- Heller, P. L., Komar, P. D., & Pevear, D. R. (1980). Transport processes in ooid genesis. *Journal of Sedimentary Research*, 50(3).
- Higgins, M. D. (2000). Measurement of crystal size distributions. *American Mineralogist*, 85(9), 1105–1116.
- Jaquet, C., Andó, E., Viggiani, G., & Talbot, H. (2013). Estimation of separating planes between touching 3D objects using power watershed. In *International Symposium on Mathematical Morphology and Its Applications to Signal and Image Processing* (pp. 452–463).
- Kellerhals, R., Shaw, J., & Arora, V. K. (1975). On grain size from thin sections. *The Journal of Geology*, 83(1), 79–96.
- Krumbein, W. (1935). Thin-section mechanical analysis of indurated sediments. *The Journal of Geology*, 43(5), 482–496.
- Lehrmann, D. J., Minzoni, M., Li, X., Yu, M., Payne, J. L., Kelley, B. M., et al. (2012). Lower Triassic oolites of the Nanpanjiang Basin, South China: Facies architecture, giant ooids, and diagenesis implications for hydrocarbon reservoirs. *AAPG Bulletin*, 96(8), 1389–1414.
- Li, X., Trower, E. J., Lehrmann, D. J., Minzoni, M., Kelley, B. M., Schaal, E. K., et al. (2020). Implications of giant ooids for the carbonate chemistry of Early Triassic seawater. *Geology*, 49(2), 156–161.
- Mariotti, G., Pruss, S., Summons, R., Newman, S., & Bosak, T. (2018). Contribution of benthic processes to the growth of ooids on a low-energy shore in Cat Island, The Bahamas. *Minerals*, 8(6), 252.
- Mehra, A., & Maloof, A. (2018). Multiscale approach reveals that *Cloudina* aggregates are detritus and not in situ reef constructions. *Proceedings of the National Academy of Sciences*, 115(11), E2519–E2527.
- Mehra, A., Watters, W. A., Grotzinger, J. P., & Maloof, A. C. (2020). Three-dimensional reconstructions of the putative metazoan *Namapoikia* show that it was a microbial construction. *Proceedings of the National Academy of Sciences*, 117(33), 19760–19766.
- Newell, N. D., Purdy, E. G., & Imbrie, J. (1960). Bahamian oölitic sand. *The Journal of Geology*, 68(5), 481–497.
- Novák-Szabó, T., Sipos, A. Á., Shaw, S., Bertoni, D., Pozzebon, A., Grottole, E., et al. (2018). Universal characteristics of particle shape evolution by bed-load chipping. *Science Advances*, 4(3), ea04946. <https://doi.org/10.1126/sciadv.a04946>
- Opdyke, B. N., & Wilkinson, B. H. (1990). Paleolatitude distribution of Phanerozoic marine ooids and cements. *Palaeogeography, Palaeoclimatology, Palaeoecology*, 78(1–2), 135–148.
- Peterson, T. D. (1996). A refined technique for measuring crystal size distributions in thin section. *Contributions to Mineralogy and Petrology*, 124(3–4), 395–405.
- Pierret, A., Capowiez, Y., Belzunces, L., & Moran, C. (2002). 3D reconstruction and quantification of macropores using X-ray computed tomography and image analysis. *Geoderma*, 106(3–4), 247–271.
- Prager, E. J., Southard, J. B., & Vivoni-Gallart, E. R. (1996). Experiments on the entrainment threshold of well-sorted and poorly sorted carbonate sands. *Sedimentology*, 43(1), 33–40.
- Rose, C. V., Maloof, A. C., Schoene, B., Ewing, R. C., Linnemann, U., Hofmann, M., & Cottle, J. M. (2013). The end-Cryogenian glaciation of South Australia. *Geoscience Canada*, 40(4), 256–293.
- Sahagian, D. L., & Proussevitch, A. A. (1998). 3D particle size distributions from 2D observations: Stereology for natural applications. *Journal of Volcanology and Geothermal Research*, 84(3–4), 173–196.
- Sandberg, P. A. (1983). An oscillating trend in Phanerozoic non-skeletal carbonate mineralogy. *Nature*, 305(5929), 19–22.

- Siadatmousavi, S. M., & Jose, F. (2015). Winter storm-induced hydrodynamics and morphological response of a shallow transgressive shoal complex: Northern Gulf of Mexico. *Estuarine, Coastal and Shelf Science*, *154*, 58–68.
- Sipos, A. A., Domokos, G., & Jerolmack, D. J. (2018). Shape evolution of ooids: A geometric model. *Scientific Reports*, *8*(1), 1758.
- Summer, D. Y., & Grotzinger, J. P. (1993). Numerical modeling of ooid size and the problem of Neoproterozoic giant ooids. *Journal of Sedimentary Research*, *63*(5).
- Trower, E. J. (2020). The enigma of Neoproterozoic giant ooids—fingerprints of extreme climate?. *Geophysical Research Letters*, *47*(4), e2019GL086146.
- Trower, E. J., Bridgers, S. L., Lamb, M. P., & Fischer, W. W. (2020). Ooid cortical stratigraphy reveals common histories of individual co-occurring sedimentary grains. *Journal of Geophysical Research: Earth Surface*, *125*(7), e2019JF005452. <https://doi.org/10.1029/2019JF005452>
- Trower, E. J., Cantine, M. D., Gomes, M. L., Grotzinger, J. P., Knoll, A. H., Lamb, M. P., et al. (2018). Active ooid growth driven by sediment transport in a high-energy shoal, Little Ambergris Cay, Turks and Caicos Islands. *Journal of Sedimentary Research*, *88*(9), 1132–1151.
- Trower, E. J., Lamb, M. P., & Fischer, W. W. (2017). Experimental evidence that ooid size reflects a dynamic equilibrium between rapid precipitation and abrasion rates. *Earth and Planetary Science Letters*, *468*, 112–118.
- Wanless, H., & Dravis, J. (1989). Carbonate environments and sequences of Caicos Platform. In *28th International Geological Congress, American Geophysical Union, Field Trip Guidebook* (Vol. 374).
- Wilkinson, B. H., & Given, R. K. (1986). Secular variation in abiogenic marine carbonates: Constraints on Phanerozoic atmospheric carbon dioxide contents and oceanic Mg/Ca ratios. *The Journal of Geology*, *94*(3), 321–333.